Skeletonized wave-equation inversion for Q

Gaurav Dutta* and Gerard T. Schuster, King Abdullah University of Science and Technology

A wave-equation gradient optimization method is presented that inverts for the subsurface Q distribution by minimizing a skeletonized misfit function ε. Here, ε is the sum of the squared differences between the observed and the predicted peak/centroid frequency shifts of the early-arrivals. The gradient is computed by migrating the observed traces weighted by the frequency-shift residuals. The background Q model is perturbed until the predicted and the observed traces have the same peak frequencies or the same centroid frequencies. Numerical tests show that an improved accuracy of the inverted Q model by wave-equation Q tomography (WQ) leads to a noticeable improvement in the migration image quality.

INTRODUCTION

The real earth is anelastic and distorts the amplitude and the phase of a propagating seismic wave (Aki and Richards, 1980). Attenuation of P-waves can be quantified by a quality factor Q which accounts for the phase shift as a function of the frequency content of the propagating waves and the distance traveled.

The amplitude loss due to attenuation is often compensated for during prestack depth migration (PSDM). For example, Xin et al. (2008) and Xie et al. (2009) compensated for the attenuation loss by ray-tracing methods. Dai and West (1994), Yu et al. (2002), Wang (2008) and Valenciano et al. (2011) used one-way wave-equation migration in the frequency domain for attenuation compensation. For reverse time migration (RTM), Zhang et al. (2010), Suh et al. (2012), Fletcher et al. (2012), Bai et al. (2013), Zhu et al. (2014) and Zhu and Harris (2015) proposed different visco-acoustic wave equations with separate controls over phase and amplitude to compensate for the attenuation loss. Dutta and Schuster (2014) and Sun et al. (2015) used anelastic least-squares RTM (LSRTM) schemes to successfully compensate for the amplitude loss and the phase distortion because of Q during migration.

Besides velocity, an additional input requirement for these Q-based migration algorithms is a reliable estimate of the background Q model. A Q model can be either estimated using data-domain or image-domain based tomography techniques. In the data-domain, Brzostowski and McMechan (1992) used the attenuation of amplitudes as the input data for Q tomography. In contrast, Quan and Harris (1997) used the frequency-shifts between the predicted and the observed traces and smeared the shifts along raypaths to update the Q model. A similar adaptive centroid frequency-shift approach was also used by He et al. (2013). These frequency-shift methods rely on the high-frequency assumption made in classical ray-based tomography. Alternative data-domain approaches include using a FWI-like algorithm where an objective function is set up to invert for a Q model that minimizes the L2 norm of the residual between the observed and the predicted data (Bai et al., 2013; Wang and Zhang, 2014).

For the image-domain based Q tomography techniques, a residual image is usually minimized, which is the difference between the image computed by the background Q model and a target image, which is attenuation-free (Zhou et al., 2011; Shen et al., 2014; Shen and Zhu, 2015; Shen et al., 2015). The image perturbation is then related to the perturbation in Q using ray-based or wave-equation based tomography operators.

In this paper, we present a new skeletonized wave-equation Q inversion method that is based on minimizing the difference between the peak frequencies of the observed and the predicted transmission arrivals. The peak frequencies are obtained from the amplitude spectra of the traces, which are a skeletonized representation of the data. Unlike conventional ray-based Q tomography, the WQ residuals are smeared along transmission wavepaths (Woodward, 1992) computed from finite-difference solutions to the time-domain visco-acoustic wave equation characterized by the standard linear solid (SLS) mechanism (Carcione et al., 1988; Blanch et al., 1995). The proposed approach has no high-frequency assumptions about the data unlike ray-based tomography methods and is also less susceptible to cycle-skipping problems associated with any FWI-like algorithm.

THEORY

In our analysis, we assume that the wave propagation honors the 2D time-domain visco-acoustic wave equation based on the SLS mechanism (Blanch et al., 1995). For a given velocity and Q model, the pressure seismograms can be computed by

$$
\begin{aligned}
&\frac{\partial P}{\partial t} + K(\tau+1)(\nabla \cdot \mathbf{v}) + r_p = S(\mathbf{x}_s, t), \\
&\frac{\partial \mathbf{v}}{\partial t} + \frac{1}{\rho}\nabla P = 0, \\
&\frac{\partial r_p}{\partial t} + \frac{1}{\tau_\sigma}\left(r_p + \tau K(\nabla \cdot \mathbf{v})\right) = 0.
\end{aligned}
\tag{1}
$$

Here, $\mathbf{v} = \{v_x, v_y, v_z\}$ represents the particle velocity vector, P represents pressure, r_p represents the memory variable, K represents the bulk modulus of the medium and $S(\mathbf{x}_s, t)$ represents a bandlimited point source function at $\mathbf{x} = \mathbf{x}_s$. The parameter τ is related to the stress and the strain relaxation parameters, τ_σ and τ_ε, and the quality factor, Q as

$$
\tau_\sigma = \frac{\sqrt{1 + \frac{1}{Q^2}} - \frac{1}{Q}}{\omega}, \quad \tau_\varepsilon = \frac{\sqrt{1 + \frac{1}{Q^2}} + \frac{1}{Q}}{\omega},
$$

$$
\tau = \frac{\tau_\varepsilon}{\tau_\sigma} - 1 = \frac{2}{Q}\left(\frac{1}{Q} + \sqrt{1 + \frac{1}{Q^2}}\right).
\tag{2}
$$

Here, ω is the reference angular frequency and is usually chosen to be the central frequency of the source wavelet (Robertsson et al., 1994). For the parameterization in WQ, the parameter τ is used and the updates in τ are mapped to Q using equation 2.

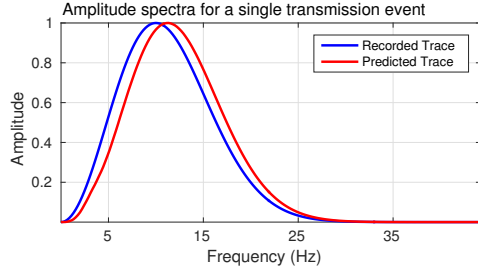Amplitude spectra for a single transmission event

Figure 1: Comparison between the amplitude spectra of a single transmission arrival in a predicted and an observed trace.

The key steps in WQ are: (1) define a connective function (Luo and Schuster, 1991) that connects the frequency-shift residuals with the pressure seismograms, (2) define a frequency-shift misfit function, and (3) derive the perturbation of the misfit function with respect to Q using the connective function and the visco-acoustic wave equation in equation 1. These steps are discussed in the following sub-sections.

Connective function

Let $\tilde{P}_f(\mathbf{x}_r, t; \mathbf{x}_s)$ denote a predicted event for a given background Q model recorded at the receiver location $\mathbf{x}_r$ due to a source excited at time $t = 0$ and at location $\mathbf{x}_s$. f is the peak frequency of this event that can be obtained from its amplitude spectrum (shown by the red curve in Figure 1). Similarly, let $P_{f-\Delta f}(\mathbf{x}_r, t; \mathbf{x}_s)$ denote the same event in the observed data (the spectrum of this event is shown by the blue curve in Figure 1). Δf is the shift between the peak frequencies of the predicted and the observed traces because of Q.

For the right background velocity model, the similarity between the amplitude-normalized observed and predicted traces in Figure 2 can be written as

$$F_f(\mathbf{x}_r, t; \mathbf{x}_s) = \int dt \ \frac{P_{f-\Delta f}(\mathbf{x}_r, t; \mathbf{x}_s)}{A_1(\mathbf{x}_r; \mathbf{x}_s)} \frac{\tilde{P}_f(\mathbf{x}_r, t; \mathbf{x}_s)}{A_2(\mathbf{x}_r; \mathbf{x}_s)},$$

$$= \int dt \ \frac{P_{f-\Delta f}(\mathbf{x}_r, t; \mathbf{x}_s)}{A(\mathbf{x}_r; \mathbf{x}_s)} \tilde{P}_f(\mathbf{x}_r, t; \mathbf{x}_s). \quad (3)$$

Here, $A_1(\mathbf{x}_r; \mathbf{x}_s)$ and $A_2(\mathbf{x}_r; \mathbf{x}_s)$ are the amplitude normalization factors for the observed and the predicted events, respectively, and $A(\mathbf{x}_r; \mathbf{x}_s) = A_1(\mathbf{x}_r; \mathbf{x}_s) A_2(\mathbf{x}_r; \mathbf{x}_s)$. These factors normalize the events to a maximum amplitude of 1 such that only the shift in peak frequency is emphasized upon by the cross-correlation function in equation 3.

In WQ, only the peak frequency-shift between an observed and a predicted trace is minimized. If $f = \Delta f$ represents the peak-frequency shift for the right background Q model, then the predicted and the observed arrivals will have the same peak frequency and the normalized cross-correlation function in equation 3 will be maximized. The derivative of $F_f(\mathbf{x}_r, t; \mathbf{x}_s)$ with respect to f should then be zero at $f = \Delta f$. Thus,

$$\dot{F}_{\Delta f} = \left[\frac{\partial F_f(\mathbf{x}_r, t; \mathbf{x}_s)}{\partial f} \right]_{f=\Delta f}$$

$$= \int dt \ \frac{\dot{P}_{f-\Delta f}(\mathbf{x}_r, t; \mathbf{x}_s)}{A(\mathbf{x}_r; \mathbf{x}_s)} \tilde{P}_f(\mathbf{x}_r, t; \mathbf{x}_s) = 0, \quad (4)$$
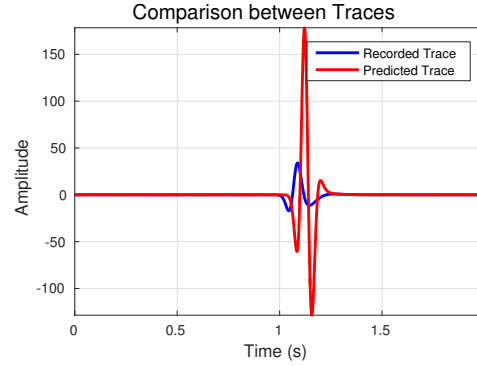
Comparison between Traces

Figure 2: Comparison between a predicted and an observed trace for a single transmission arrival.

where $\dot{P}_f(\mathbf{x}_r, t; \mathbf{x}_s) = \partial P_f(\mathbf{x}_r, t; \mathbf{x}_s)/\partial f$. Equation 4 is the connective function which will be later used to derive the Fréchet derivative of τ.

Misfit function

The WQ method attempts to invert for a Q model or an equivalent τ model which predicts pressure seismograms $\tilde{P}_f(\mathbf{x}_r, t; \mathbf{x}_s)$ that minimize the misfit function

$$\varepsilon = \frac{1}{2} \sum_s \sum_r \Delta f(\mathbf{x}_r, \mathbf{x}_s)^2, \quad (5)$$

where Δf is defined in the previous sub-section and the summation in equation 5 is over all sources and receivers. Using the implicit function theorem for the connective function $\dot{F}_{\Delta f}(\Delta f, \tau)$, the gradient $\gamma(\mathbf{x})$ is given by

$$\gamma(\mathbf{x}) = -\frac{\partial \varepsilon}{\partial \tau(\mathbf{x})} = -\sum_s \sum_r \frac{\partial \Delta f}{\partial \tau(\mathbf{x})} \Delta f(\mathbf{x}_r, \mathbf{x}_s) = \sum_s \sum_r \frac{\frac{\partial \dot{F}_{\Delta f}}{\partial \tau(\mathbf{x})}}{\frac{\partial \dot{F}_{\Delta f}}{\partial \Delta f}} \Delta f(\mathbf{x}_r, \mathbf{x}_s). \quad (6)$$

From equation 4 we also get the following 2 equations:

$$\frac{\partial \dot{F}_{\Delta f}}{\partial \Delta f} = \int dt \frac{\ddot{P}_{f-\Delta f}(\mathbf{x}_r, t; \mathbf{x}_s)}{A(\mathbf{x}_r; \mathbf{x}_s)} \tilde{P}_f(\mathbf{x}_r, t; \mathbf{x}_s), \quad (7)$$

$$\frac{\partial \dot{F}_{\Delta f}}{\partial \tau(\mathbf{x})} = \int dt \frac{\dot{P}_{f-\Delta f}(\mathbf{x}_r, t; \mathbf{x}_s)}{A(\mathbf{x}_r; \mathbf{x}_s)} \frac{\partial \tilde{P}_f(\mathbf{x}_r, t; \mathbf{x}_s)}{\partial \tau(\mathbf{x})}. \quad (8)$$

The Fréchet derivative $\frac{\partial \tilde{P}_f(\mathbf{x}_r, t; \mathbf{x}_s)}{\partial \tau(\mathbf{x})}$ is now derived in the next subsection.

Fréchet derivative

To obtain the Fréchet derivative of the pressure field with respect to the perturbation in $\tau(\mathbf{x})$, we linearize the visco-acoustic wave equation in equation 1. A perturbation of $\tau \to \tau + \delta\tau$ will produce perturbed wavefields $\delta\tilde{P}_f$, $\delta\mathbf{v}$ and δr_p which satisfy the linearized visco-acoustic wave equation given by

$$\frac{\partial \delta\tilde{P}_f}{\partial t} + K(\tau + 1)(\nabla \cdot \delta\mathbf{v}) + \delta r_p = -K\delta\tau(\nabla \cdot \mathbf{v}),$$

$$\frac{\partial \delta\mathbf{v}}{\partial t} + \frac{1}{\rho}\nabla\delta\tilde{P}_f = 0,$$

$$\frac{\partial \delta r_p}{\partial t} + \frac{1}{\tau_\sigma}\left(\delta r_p + \tau K(\nabla \cdot \delta\mathbf{v})\right) = -\frac{K}{\tau_\sigma}\delta\tau(\nabla \cdot \mathbf{v}). \quad (9)$$

Using the Green's functions $g_P(\mathbf{x}_r,t;\mathbf{x},0)$ and $g_{r_p}(\mathbf{x}_r,t;\mathbf{x},0)$, the Fréchet derivative $\frac{\partial \tilde{P}_f(\mathbf{x}_r,t;\mathbf{x}_s)}{\partial \tau(\mathbf{x})}$ can be expressed as

$$\frac{\partial \tilde{P}_f(\mathbf{x}_r,t;\mathbf{x}_s)}{\partial \tau(\mathbf{x})} = -(K(\mathbf{x})(g_P(\mathbf{x}_r,t;\mathbf{x},0) * \nabla \cdot \mathbf{v}(\mathbf{x},t;\mathbf{x}_s))$$
$$+ \frac{K(\mathbf{x})}{\tau_\sigma(\mathbf{x})}(g_{r_p}(\mathbf{x}_r,t;\mathbf{x},0) * \nabla \cdot \mathbf{v}(\mathbf{x},t;\mathbf{x}_s))). \quad (10)$$

where $*$ denotes convolution in time. Here, $g_p(\mathbf{x}_r,t;\mathbf{x})$ and $g_{r_p}(\mathbf{x}_r,t;\mathbf{x})$ are the pressure and the memory variable Green's functions, respectively, and $\mathbf{v}$ is the particle velocity vector in equation 1. Equation 8 can now be written as

$$\frac{\partial \dot{F}_{\Delta f}}{\partial \tau(\mathbf{x})} = \int dt \, \frac{\dot{P}_{f-\Delta f}(\mathbf{x}_r,t;\mathbf{x}_s)}{A(\mathbf{x}_r;\mathbf{x}_s)} \frac{\partial \tilde{P}_f(\mathbf{x}_r,t;\mathbf{x}_s)}{\partial \tau(\mathbf{x})}$$
$$= -\int dt \, K(\mathbf{x})(g_P(\mathbf{x}_r,t;\mathbf{x},0) * \nabla \cdot \mathbf{v}(\mathbf{x},t;\mathbf{x}_s)$$
$$+ \frac{g_{r_p}(\mathbf{x}_r,t;\mathbf{x},0)}{\tau_\sigma(\mathbf{x})} * \nabla \cdot \mathbf{v}(\mathbf{x},t;\mathbf{x}_s)) \frac{\dot{P}_{f-\Delta f}(\mathbf{x}_r,t;\mathbf{x}_s)}{A(\mathbf{x}_r;\mathbf{x}_s)}. \quad (11)$$

Substituting equations 7 and 11 into equation 6 and using the identity $\int dt \, [f(t) * g(t)] h(t) = \int dt \, g(t) [f(-t) * h(t)]$, the gradient $\gamma(\mathbf{x})$ can be expressed as

$\gamma(\mathbf{x})$

$$= -\frac{K(\mathbf{x})}{E} \sum_s \int dt (\overbrace{\nabla \cdot \mathbf{v}(\mathbf{x},t;\mathbf{x}_s)}^{source} \overbrace{\sum_r (g_P(\mathbf{x}_r,-t;\mathbf{x},0) * \Delta P_f(\mathbf{x}_r,t;\mathbf{x}_s))}^{backpropagated\ residual}$$
$$+ \frac{1}{\tau_\sigma(\mathbf{x})} \overbrace{\nabla \cdot \mathbf{v}(\mathbf{x},t;\mathbf{x}_s)}^{source} \overbrace{\sum_r (g_{r_p}(\mathbf{x}_r,-t;\mathbf{x},0) * \Delta P_f(\mathbf{x}_r,t;\mathbf{x}_s))}^{backpropagated\ residual})$$
$$= -\frac{K(\mathbf{x})}{E} \sum_s \int dt \, \nabla \cdot \mathbf{v}(\mathbf{x},t;\mathbf{x}_s) \left(q(\mathbf{x},t;\mathbf{x}_s) + \frac{s(\mathbf{x},t;\mathbf{x}_s)}{\tau_\sigma(\mathbf{x})} \right), \quad (12)$$

where $E = \int dt \, \ddot{P}_{f-\Delta f}(\mathbf{x}_r,t;\mathbf{x}_s) \tilde{P}_f(\mathbf{x}_r,t;\mathbf{x}_s)$ and $\Delta P_f(\mathbf{x}_r,t;\mathbf{x}_s) = \dot{P}_{f-\Delta f}(\mathbf{x}_r,t;\mathbf{x}_s) \Delta f(\mathbf{x}_r,\mathbf{x}_s)$ denotes the data residual obtained by weighting the observed traces with the residual frequency-shifts. q and s are the adjoint-state variables of P and r_p, respectively. The gradient in equation 12 can be numerically computed by a zero-lag cross-correlation of a forward propagated source wavefield term $\nabla \cdot \mathbf{v}(\mathbf{x},t;\mathbf{x}_s)$ and backpropagated residual wavefield terms $q(\mathbf{x},t;\mathbf{x}_s)$ and $s(\mathbf{x},t;\mathbf{x}_s)$. The residual wavefields are computed by using the data residual as adjoint sources from the receiver side.

For diving waves, where there are more than one event present, the peak frequency for the arrivals cannot be accurately estimated since each arrival has its own peak frequency. In such cases, the objective function in equation 5 can be modified to minimize the centroid frequency-shifts between the predicted and the observed traces as

$$\varepsilon = \frac{1}{2} \sum_s \sum_r \Delta f_{centroid}(\mathbf{x}_r,\mathbf{x}_s)^2,$$
$$= \frac{1}{2} \sum_s \sum_r \left(\frac{\int_0^f f_p A(f_p)}{\int_0^f A(f_p)} - \frac{\int_0^f f_o A(f_o)}{\int_0^f A(f_o)} \right)^2. \quad (13)$$
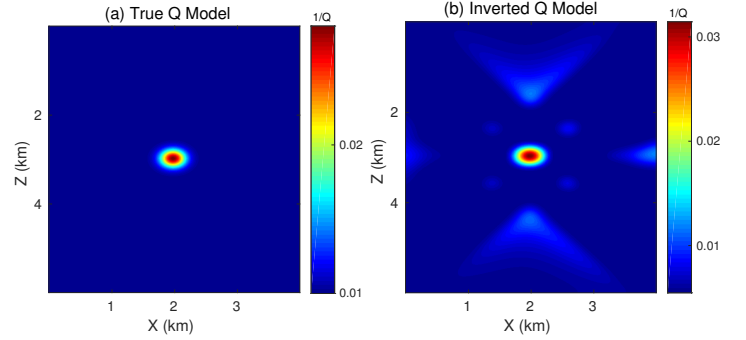

Figure 3: (a) True Q model, and (b) inverted Q model using WQ.

The subscripts o and p stand for observed and predicted, respectively, and $A(f)$ is the amplitude for a frequency f. The gradient for this objective function can be similarly derived as shown in the previous sub-sections.

NUMERICAL RESULTS

The effectiveness of WQ is first demonstrated on a simple synthetic example. Figure 3(a) shows a homogeneous model with a velocity of 2 km/s. A Gaussian Q anomaly is embedded at the center of the model. The maximum Q at the center of the anomaly is 40. The source and the receiver wells are offset by 4 km and there are 60 evenly spaced sources in the source well and 200 evenly spaced receivers in the receiver well. For WQ, the starting Q model is taken to be homogeneous with Q=1000. Figure 3(b) shows the final Q tomogram obtained from WQ. It is evident that the Gaussian Q anomaly is successfully reconstructed by WQ.

The WQ method is now tested on a more complex 2D section of the 3D SEG/EAGE overthrust model. Figures 4(a) and 4(b) show the true velocity and Q models, respectively, used for generating the observed data. The inverted Q tomogram after 35 iterations is shown in Figure 4(d). It is evident that WQ can successfully recover the low-intermediate wavenumber details of the background Q model. The fidelity of the Q tomogram is validated by a comparison between the acoustic RTM, acoustic LSRTM, Q-RTM and Q-LSRTM images (Dutta and Schuster, 2014) in Figure 5. It is evident that the inverted Q tomogram from WQ can be used as the background Q model for any Q-PSDM algorithm to obtain images with better resolution and better balanced amplitudes than standard migration techniques.

As a final example, WQ is applied to the Friendswood crosswell data (Chen et al., 1990). The starting Q model is taken to be homogeneous with Q=1000 and the early-arrival FWI tomogram, shown in Figure 6(a), is used as the background velocity model. The Q tomogram obtained after 30 iterations is shown in Figure 6(b). There is a good agreement geologically between the velocity and the Q tomograms. The high attenuation regions in the Q tomogram correspond to the low velocity regions in the FWI tomogram.
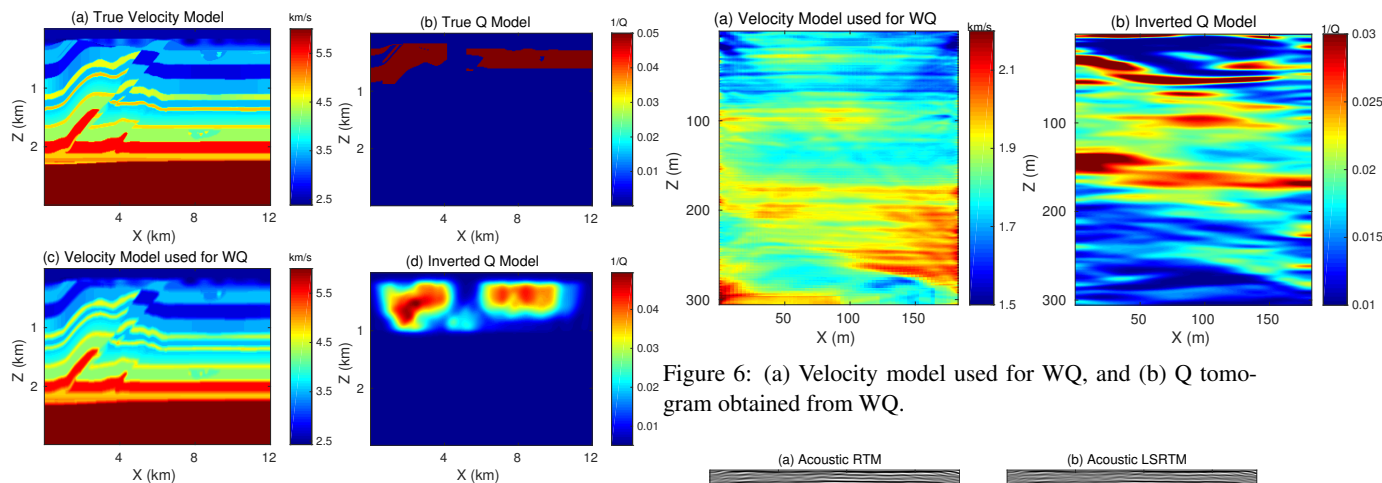
Figure 4: a) True velocity, and (b) Q models used for generating the observed data, (c) velocity model used for WQ, and (d) inverted Q tomogram from WQ.

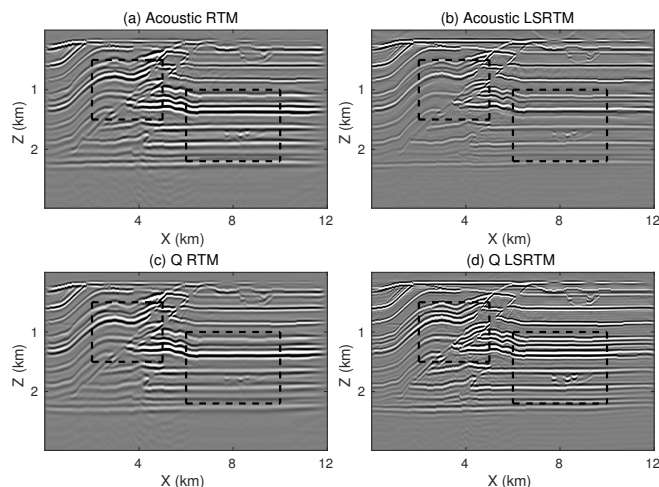Figure 6: (a) Velocity model used for WQ, and (b) Q tomogram obtained from WQ.

Figure 5: Acoustic (a) RTM, and (b) LSRTM images obtained from the visco-acoustic data. (c) Q-RTM, and (d) Q-LSRTM images for the same data using the tomogram obtained from WQ as the background Q model. The black boxes delineate the areas where improvements in imaging can be seen with WQ and Q-LSRTM.

The Q-LSRTM image, shown in Figure 7(d), is obtained by using the velocity and the WQ tomograms in Figure 6. Similar to the synthetic example, the Q-LSRTM image using the WQ tomogram has events with better balanced amplitudes than the standard RTM and LSRTM images in Figures 7(a) and 7(b), respectively.

CONCLUSIONS

A novel wave-equation Q tomography method is presented where a skeletonized representation of the data, i.e., the difference between the peak frequencies or the centroid frequen-
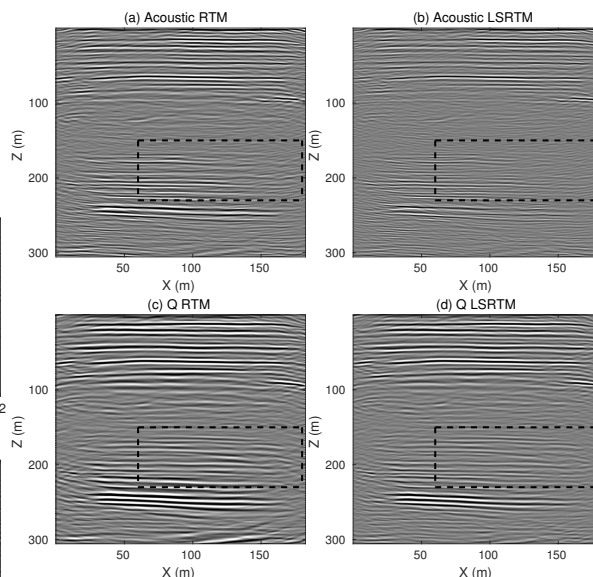

Figure 7: Images from (a) acoustic RTM, (b) acoustic LSRTM, (c) Q-RTM, and (d) Q-LSRTM for the crosswell field data using the Q tomogram obtained from WQ. The black boxes delineate the areas where improvements in imaging can be seen.

cies of the observed and the predicted arrivals are inverted to estimate the background Q model. The gradient for WQ is obtained by a zero-lag cross-correlation between the forward propagated source wavefield and the backprojected observed pressure seismograms that are weighted by the frequency-shifts. Numerical results on synthetic and field data demonstrate that if the recorded data suffer from strong attenuation, the WQ method can be used to estimate the background Q model. The inverted Q tomogram can be used with any Q-PSDM algorithm to obtain images with balanced amplitudes and high resolution in areas where there is strong attenuation.

ACKNOWLEDGEMENTS

REFERENCES

Aki, K., and P. G. Richards, 1980, Quantitative seismology: Freeman Publication Co.

Bai, J., G. Chen, D. Yingst, and J. Leveille, 2013, Attenuation compensation in viscoacoustic reverse time migration: 83rd Annual International Meeting, SEG, Expanded Abstracts, **740**, 3825–3830, http://dx.doi.org/10.1190/segam2013-1252.1.

Blanch, J. O., J. O. Robertsson, and W. W. Symes, 1995, Modeling of a constant Q: Methodology and algorithm for an efficient and optimally inexpensive viscoelastic technique: Geophysics, **60**, 176–184, http://dx.doi.org/10.1190/1.1443744.

Brzostowski, M. A., and G. A. McMechan, 1992, 3D tomographic imaging of near-surface seismic velocity and attenuation: Geophysics, **57**, 396–403, http://dx.doi.org/10.1190/1.1443254.

Carcione, J. M., D. Kosloff, and R. Kosloff, 1988, Wave propagation simulation in a linear viscoacoustic medium: Geophysical Journal International, **93**, 393–401, http://dx.doi.org/10.1111/j.1365-246X.1988.tb02010.x.

Chen, S., L. Zimmerman, and J. Tugnait, 1990, Subsurface imaging using reversed vertical seismic profiling and crosshole tomographic methods: Geophysics, **55**, 1478–1487, http://dx.doi.org/10.1190/1.1442795.

Dai, N., and G. West, 1994, Inverse Q migration: 64th Annual International Meeting, SEG, Expanded Abstracts, **389**, 1418–1421, http://dx.doi.org/10.1190/1.1822799.

Dutta, G., and G. T. Schuster, 2014, Attenuation compensation for least-squares reverse time migration using the viscoacoustic-wave equation: Geophysics, **79**, no. 6, S251–S262, http://dx.doi.org/10.1190/geo2013-0414.1.

Fletcher, R. P., D. Nichols, and M. Cavalca, 2012, Wavepath consistent effective Q estimation for Q-compensated reverse time migration: 74th Annual International Conference and Exhibition, EAGE, Extended Abstracts, A020.

He, Y., K. Xin, and Y. Xie, 2013, 3D Q tomographic inversion using adaptive centroid frequency shift for compensating absorption and dispersion: EAGE Workshop on Seismic Attenuation, EAGE, http://dx.doi.org/10.3997/2214-4609.20131848.

Luo, Y., and G. T. Schuster, 1991, Wave-equation traveltime inversion: Geophysics, **56**, 645–653, http://dx.doi.org/10.1190/1.1443081.

Quan, Y., and J. M. Harris, 1997, Seismic attenuation tomography using the frequency shift method: Geophysics, **62**, 895–905, http://dx.doi.org/10.1190/1.1444197.

Robertsson, J. O., J. O. Blanch, and W. W. Symes, 1994, Viscoelastic finite-difference modeling: Geophysics, **59**, 1444–1456, http://dx.doi.org/10.1190/1.1443701.

Shen, Y., B. Biondi, and R. Clapp, 2015, Wave-equation based Q tomography from angle-domain common image gathers: 85th Annual International Meeting, SEG, Expanded Abstracts, **829**, 4334–4338, http://dx.doi.org/10.1190/segam2015-5917329.1.

Shen, Y., B. Biondi, R. Clapp, and D. Nichols, 2014, Wave-equation migration Q analysis (WEMQA): 84th Annual International Meeting, SEG, Expanded Abstracts, **718**, 3757–3762, http://dx.doi.org/10.1190/segam2014-1557.1.

Shen, Y., and T. Zhu, 2015, Image-based Q tomography using reverse time Q migration: 85th Annual International Meeting, SEG, Expanded Abstracts, **708**, 3694–3698, http://dx.doi.org/10.1190/segam2015-5852526.1.

Suh, S., K. Yoon, J. Cai, and B. Wang, 2012, Compensating visco-acoustic effects in anisotropic resverse-time migration: 82nd Annual International Meeting, SEG, Expanded Abstracts, **649**, 1–5, http://dx.doi.org/10.1190/segam2012-1297.1.

Sun, J., S. Fomel, and T. Zhu, 2015, Preconditioning least-squares RTM in viscoacoustic media by *Q*-compensated RTM: 85th Annual International Meeting, SEG, Expanded Abstracts, **758**, 3959–3965, http://dx.doi.org/10.1190/segam2015-5880944.1.

Valenciano, A., N. Chemingui, D. Whitmore, and S. Brandsberg-Dahl, 2011, Wave equation migration with attenuation and anisotropy compensation: 81st Annual International Meeting, SEG, Expanded Abstracts, **45**, 232–236, http://dx.doi.org/10.1190/1.3627674.

Wang, Y., 2008, Inverse Q-filtered migration: Geophysics, **73**, no. 1, S1–S6, http://dx.doi.org/10.1190/1.2806924.

Wang, Y., and J. Zhang, 2014, Pseudo 2D elastic waveform inversion for Q factor in the near surface: 84th Annual International Meeting, SEG, Expanded Abstracts, **386**, 2019–2023, http://dx.doi.org/10.1190/segam2014-1053.1.

Woodward, M. J., 1992, Wave-equation tomography: Geophysics, **57**, 15–26, http://dx.doi.org/10.1190/1.1443179.

Xie, Y., K. Xin, J. Sun, C. Notfors, A. K. Biswal, and M. K. Balasubramaniam, 2009, 3D prestack depth migration with compensation for frequency dependent absorption and dispersion: 79th Annual International Meeting, SEG, Expanded Abstracts, **586**, 2919–2923, http://dx.doi.org/10.1190/1.3255457.

Xin, K., B. Hung, S. Birdus, and J. Sun, 2008, 3D tomographic amplitude inversion for compensating amplitude attenuation in the overburden: 78th Annual International Meeting, SEG, Expanded Abstracts, **652**, 3239–3243, http://dx.doi.org/10.1190/1.3064018.

Yu, Y., R. Lu, and M. Deal, 2002, Compensation for the effects of shallow gas attenuation with viscoacoustic wave equation migration: 72nd Annual International Meeting, SEG, Expanded Abstracts, **523**, 2062–2065, http://dx.doi.org/10.1190/1.1817107.

Zhang, Y., P. Zhang, and H. Zhang, 2010, Compensating for visco-acoustic effects in reverse-time migration: 80th Annual International Meeting, SEG, Expanded Abstracts, **619**, 3160–3164, http://dx.doi.org/10.1190/1.3513503.

Zhou, J., S. Birdus, B. Hung, K. H. Teng, Y. Xie, D. Chagalov, A. Cheang, D. Wellen, and J. Garrity, 2011, Compensating attenuation due to shallow gas through Q tomography and Q-PSDM, a case study in Brazil: 81st Annual International Meeting, SEG, Expanded Abstracts, **650**, 3332–3336, http://dx.doi.org/10.1190/1.3627889.

Zhu, T., and J. M. Harris, 2015, Improved seismic image by *Q*-compensated reverse time migration: Application to crosswell field data, west Texas: Geophysics, **80**, no. 2, B61–B67, http://dx.doi.org/10.1190/geo2014-0463.1.

Zhu, T., J. M. Harris, and B. Biondi, 2014, *Q*-compensated reverse-time migration: Geophysics, **79**, no. 3, S77–S87, http://dx.doi.org/10.1190/geo2013-0344.1.